AMERICAN SOCIETY FOR MICROBIOLOGY | Journal of Virology®

VIRUS-CELL INTERACTIONS

Sphingomyelin-Sequestered Cholesterol Domain Recruits Formin-Binding Protein 17 for Constricting Clathrin-Coated Pits in Influenza Virus Entry

Bo Tang,[a] En-Ze Sun,[a] Zhi-Ling Zhang,[a] Shu-Lin Liu,[b] Jia Liu,[c,d] Akihiro Kusumi,[e] Zhi-Hong Hu,[c] Tao Zeng,[a] Ya-Feng Kang,[a] Hong-Wu Tang,[a] Dai-Wen Pang[a,b]

[a]College of Chemistry and Molecular Sciences, State Key Laboratory of Virology, Wuhan University, Wuhan, People's Republic of China
[b]State Key Laboratory of Medicinal Chemical Biology, Tianjin Key Laboratory of Biosensing and Molecular Recognition, Frontiers Science Center for New Organic Matter, Research Center for Analytical Sciences, College of Chemistry, Frontiers Science Center for Cell Responses, Nankai University, Tianjin, People's Republic of China
[c]State Key Laboratory of Virology, Wuhan Institute of Virology, Chinese Academy of Sciences, Wuhan, People's Republic of China
[d]Department of Forensic Medicine, Tongji Medical College of Huazhong University of Science and Technology, Wuhan, People's Republic of China
[e]Membrane Cooperativity Unit, Okinawa Institute of Science and Technology Graduate University, Okinawa, Japan

ABSTRACT Influenza A virus (IAV) is a global health threat. The cellular endocytic machineries harnessed by IAV remain elusive. Here, by tracking single IAV particles and quantifying the internalized IAV, we found that sphingomyelin (SM)-sequestered cholesterol, but not accessible cholesterol, is essential for the clathrin-mediated endocytosis (CME) of IAV. The clathrin-independent endocytosis of IAV is cholesterol independent, whereas the CME of transferrin depends on SM-sequestered cholesterol and accessible cholesterol. Furthermore, three-color single-virus tracking and electron microscopy showed that the SM-cholesterol complex nanodomain is recruited to the IAV-containing clathrin-coated structure (CCS) and facilitates neck constriction of the IAV-containing CCS. Meanwhile, formin-binding protein 17 (FBP17), a membrane-bending protein that activates actin nucleation, is recruited to the IAV-CCS complex in a manner dependent on the SM-cholesterol complex. We propose that the SM-cholesterol nanodomain at the neck of the CCS recruits FBP17 to induce neck constriction by activating actin assembly. These results unequivocally show the physiological importance of the SM-cholesterol complex in IAV entry.

IMPORTANCE IAV infects cells by harnessing cellular endocytic machineries. A better understanding of the cellular machineries used for its entry might lead to the development of antiviral strategies and would also provide important insights into physiological endocytic processes. This work demonstrated that a special pool of cholesterol in the plasma membrane, SM-sequestered cholesterol, recruits FBP17 for the constriction of clathrin-coated pits in IAV entry. Meanwhile, the clathrin-independent cell entry of IAV is cholesterol independent. The internalization of transferrin, the gold-standard cargo endocytosed solely via CME, is much less dependent on the SM-cholesterol complex. These results provide new insights into IAV infection and the pathway/cargo-specific involvement of the cholesterol pool(s).

KEYWORDS sphingomyelin-cholesterol nanodomain, ostreolysin A (OlyA), formin-binding protein FBP17, clathrin-mediated endocytosis, single-virus tracking

Influenza A virus (IAV) is a global health threat. It infects cells by harnessing the cellular endocytic pathways clathrin-mediated endocytosis (CME) and caveolin-independent, clathrin-independent endocytosis (CIE) (1–3). Therefore, understanding the endocytic machineries harnessed by IAV is important for developing antiviral strategies to block IAV infection. In addition, it would provide important insights into physiological

Editor Anice C. Lowen, Emory University School of Medicine

Address correspondence to Dai-Wen Pang, dwpang@whu.edu.cn.

The authors declare no conflict of interest.

This work is dedicated to the 100th anniversary of Chemistry at Nankai University.

Received 20 October 2021
Accepted 7 January 2022
Accepted manuscript posted online 12 January 2022
Published 9 March 2022

endocytic processes (4, 5). For example, unlike the well-studied endogenous cargo of CME, transferrin (Tf), IAV exploits different protein machineries for its cell entry (6–8). This difference might be caused by the larger size of IAV. The diameter of IAV, which is approximately 100 nm, is comparable to the sizes of the clathrin-coated pits (CCPs). This might induce greater membrane tension and lead to the alteration of lipid compositions in the membrane (9). To investigate this possibility, here, we focused on the cholesterol requirements for IAV internalization because cholesterol in the plasma membrane (PM) is required for a variety of endocytic pathways (10–14).

The requirement of cholesterol for IAV internalization is not well understood, probably due to the confusion caused by three difficulties. First, quantification of internalized IAV was quite challenging (15): most methods measured the extent of IAV cell entry at much later stages and thus failed to accurately estimate the amounts of internalized IAV (16–19). Second, experimental results were often obtained without rigorously differentiating CME and CIE. Third, the existence of three separate pools of cholesterol (accessible, sphingomyelin [SM]-sequestered, and essential cholesterol pools) has been discovered only recently (20), and thus, it was neglected in previous studies.

The accessible cholesterol pool is detectable by domain 4 (D4) of perfringolysin O (21, 22) (also by D4 of anthrolysin O) (23). The SM-sequestered pool of cholesterol (also called the SM-cholesterol complex) can be identified by ostreolysin A (OlyA) (24, 25). The essential cholesterol pool is protected from D4 binding and OlyA binding, which can be removed only by methyl-β-cyclodextrin (MβCD) treatment after the accessible and SM-sequestered pools are depleted (20). The accessible pool of cholesterol is involved in many cellular processes, including hedgehog signaling (26), resistance to cytolysin formation (27), and blocking bacterial infection (28), whereas the biological function of the SM-sequestered pool of cholesterol has remained enigmatic.

In the present research, we investigated whether and how these three pools of cholesterol are involved in the internalizations of IAV and Tf. Surprisingly, we found that SM-sequestered cholesterol was essential for the CME of IAV, which represents ~75% of IAV internalization, whereas the CIE of IAV was cholesterol independent. The internalization of Tf, which is the gold standard of the cargoes endocytosed via CME, was much less dependent on the SM-cholesterol complex. The depletion of SM-sequestered cholesterol abolished formin-binding protein 17 (FBP17) recruitment to the IAV-containing clathrin-coated structure (CCS), leading to the failure of the neck constriction of the clathrin-coated pit (CCP).

RESULTS

We first established a method to quantify IAV internalization precisely, by improving a method developed previously (15) (Fig. 1A; see also Fig. S1 in the supplemental material), and to observe single IAV virions, CCSs, and accessible or SM-sequestered cholesterol in three colors almost simultaneously. For IAV internalization assays, IAV conjugated with biotin via the cleavable disulfide group was allowed to bind to the cell surface at 4°C, and the temperature was then raised to 37°C for IAV internalization. Throughout this study, Madin-Darby canine kidney (MDCK) cells and the IAV strain A/Hubei/01-MA01/1999 (H9N2) were used, and all live-cell observations were performed at 37°C unless otherwise stated.

IAV internalization is greatly suppressed by depleting the SM-sequestered cholesterol pools. The accessible and SM-sequestered pools of cholesterol in the outer leaflet of the PM were observed by incubating the cells with monomeric enhanced green fluorescent protein (mEGFP)-tagged D4 (simply called D4) and mEGFP-labeled OlyA (OlyA), respectively. Both D4 and OlyA are bound to the cell surface (only a few intracellular fluorescent spots were found) (Fig. 1B and Fig. S2A). The cholesterol levels in the PM were reduced by treating the cells with MβCD (29) and sphingomyelinase (SMase) (30). The MβCD treatment reduced the amounts of both OlyA and D4 on the PM, but the amount of bound OlyA (SM-sequestered cholesterol) decreased much slower than that of bound D4 (accessible cholesterol) (Fig. 1B and C and Fig. S2A, top). Meanwhile, the SMase treatment induced a rapid decrease of bound OlyA but not bound D4 (Fig. 1B

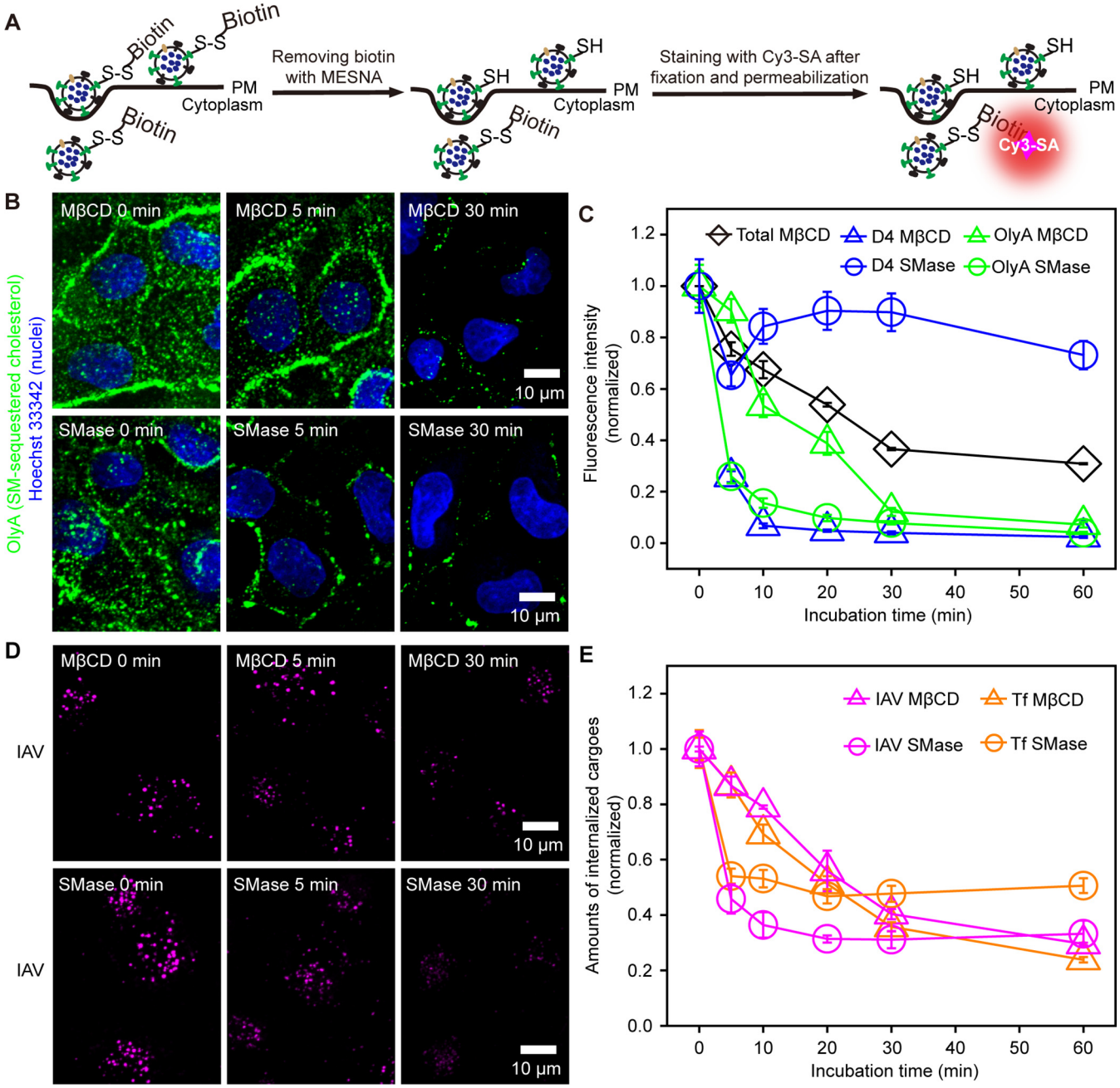

FIG 1 Depletion of SM-sequestered and accessible cholesterol suppressed IAV internalization by ~70%. (A) Experimental scheme for quantifying the amounts of internalized IAV. Biotin was removed from the IAV remaining on the cell surface using a membrane-impermeable reducer, 2-mercaptoethanesulfonate (MESNA). The removal efficiency is >99.9%, which greatly improved the precision in the estimation of internalized IAV from the previously reported method (15) (see also Fig. S1 in the supplemental material). The cells were fixed, permeabilized, and then labeled with Cy3-SA to evaluate the amounts of internalized IAV. (B) Typical confocal images (among 20 images) showing that the binding of OlyA-mEGFP (probe for SM-sequestered cholesterol) to the PM outer leaflet is decreased after MβCD (top) and SMase (bottom) treatments (time courses) (nuclei stained with Hoechst 33342 are shown in blue). (C) SMase treatment rapidly reduced OlyA-mEGFP binding (SM-sequestered cholesterol) but not mEGFP-D4 binding (accessible cholesterol). The MβCD treatment reduced both accessible and SM-sequestered cholesterol, but the accessible cholesterol is removed faster than the SM-sequestered cholesterol. The MβCD treatment employed here reduced the total cellular cholesterol in a time course similar to those reported previously (13). Errors bars represent standard errors of the means (SEMs) throughout this report. (D) Typical confocal images of internalized IAV (see panel B) in cells treated with MβCD (among 25, 23, and 23 images from left to right) and SMase (among 20 images) for 0, 5, and 30 min. (E) IAV and Tf internalizations were decreased with prolonged MβCD and SMase treatments.

and C and Fig. S2A, bottom). These results are consistent with previous observations in which SMase treatment freed the SM-sequestered cholesterol, but the level of accessible cholesterol in the PM was rather unaffected, due to the enhanced influx of the PM cholesterol into the endoplasmic reticulum (20, 25, 30, 31).

The total amount of cellular cholesterol was practically unchanged with an elongation of the MβCD treatment from 30 min to 60 min and was reduced to ~40% of that in intact cells after MβCD treatment for 60 min, similar to those reported previously (13) (Fig. 1C, black line). Moreover, the cell shape and the number density of the cells on the dish did not change after MβCD treatment for 60 min, suggesting that the amount of essential cholesterol was rather unaffected (20).

The internalizations of both IAV and Tf (tetramethylrhodamine [TMR]-labeled Tf) were reduced by ~50 to 70% after the SMase and MβCD treatments (Fig. 1D and E and Fig. S2B). Meanwhile, the internalizations of these two cargoes were not blocked completely, even under conditions where both the accessible and SM-sequestered cholesterol pools were almost totally removed from the PM (Fig. 1C). Very similar effects of these treatments were observed in other cell lines and with another IAV strain [A/Puerto Rico/8/1934 (H1N1) (PR8)] (Fig. S2C and D), suggesting that the effects of these treatments are quite general. The replenishment of cholesterol after the MβCD treatment and the replenishment of SM after the SMase treatment restored IAV internalization almost to the level before the treatments (Fig. S3A and B), implying the limited toxicity of these treatments. Meanwhile, SM addition after the MβCD treatment did not recover IAV internalization (Fig. S3C), consistent with the previous observations that MβCD treatment hardly changed the SM content in the PM (24, 30). Since both the SMase and MβCD treatments reduced IAV internalization, these results suggested that SM-sequestered cholesterol could be essential for this process (Fig. S3D).

CME of IAV is sensitive to cholesterol depletion, a finding by single-virus tracking. We quantified the CME and CIE of IAV, the well-known pathways of IAV entry (1–3, 32), by tracking single virus particles (labeled with ATTO647N) and visualizing the CCSs (marked by mEGFP-tagged clathrin light chain A [mEGFP-CLCa]). We distinguished the CME and CIE pathways by examining whether the CCS was formed at the binding site of IAV before its entry into the cell (Fig. 2A and B, Fig. S4A to C, and Movies S1 and S2), as reported previously (1, 3).

In intact cells, the CME and CIE of IAV represented 73% $\pm$ 5% and 27% $\pm$ 5% of the internalized IAV, respectively (Fig. 2C, Intact). After cholesterol depletion with MβCD for 30 min, the CME of IAV was decreased to 37% $\pm$ 7% of that in intact cells, and cholesterol replenishment restored it to the level in intact cells (Fig. 2C, Repl), showing that the CME of IAV is sensitive to either or both the accessible and SM-sequestered cholesterol pools. Meanwhile, the CIE of IAV was hardly affected by the MβCD treatment (Fig. 2C, Depl), indicating that it occurs independently of the accessible and SM-sequestered cholesterol pools. Similar results were basically reproduced in HeLa cells (Fig. S4D). These results further suggested that the CME of IAV, but not the CIE of IAV, depends on the accessible and/or SM-sequestered cholesterol pools.

IAV internalization occurs at the CCS colocalized with the SM-cholesterol complex nanodomain. We further investigated whether the SM-sequestered cholesterol pool is directly involved in the CME of IAV. For this purpose, we performed three-color observations of single virus particles (labeled by ATTO647N), CCSs (marked by mScarlet-I-CLCa), as well as accessible cholesterol (mEGFP-D4) or the SM-cholesterol complex (OlyA-mEGFP) in live cells. After IAV binds to the PM, the CCS is formed at the IAV-binding site (Fig. 2D, Fig. S4E to G, and Movie S3). The SM-cholesterol complex was often recruited to the CCS containing IAV (Fig. 3D, Fig. S4G, and Movie S3). The observed sizes of the SM-cholesterol complex were comparable to the optical diffraction limit (~250 nm). In addition, even before being recruited to the IAV-CCS complex, the signal intensities of OlyA-mEGFP spots were comparable to those of the CCSs marked by mScarlet-I-CLCa, suggesting the presence of multiple copies (probably >10 copies) of OlyA-mEGFP. These results suggest that the OlyA-mEGFP spots represent "nanodomains" of the SM-cholesterol complex.

The fraction of the IAV-CCS complex colocalized with D4 or OlyA was quantitatively evaluated by the criterion that the colocalization event lasted at least for 16 s before IAV entry. The long colocalization duration of 16 s was selected to reduce false colocalizations. The OlyA spots (SM-cholesterol complex nanodomains) were colocalized with

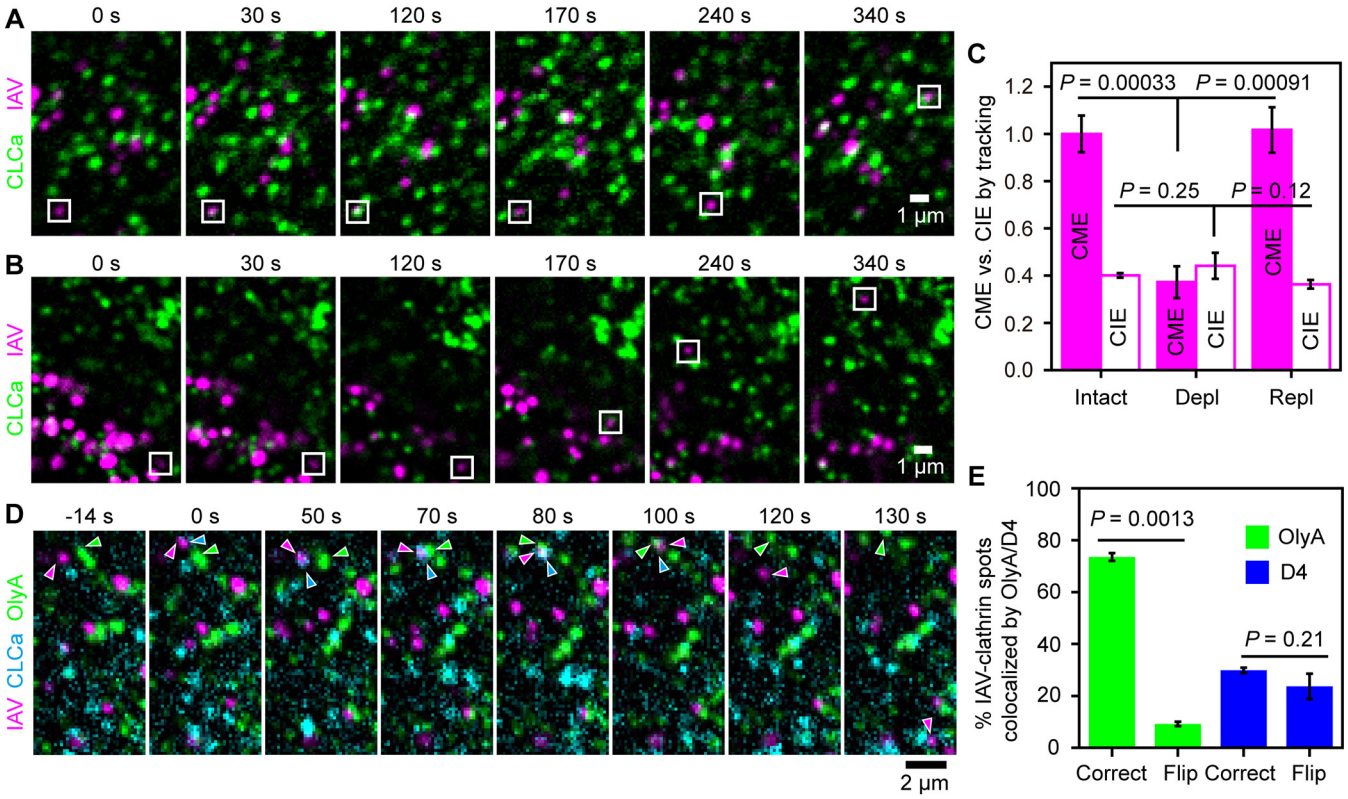

FIG 2 The SM-cholesterol complex nanodomain is recruited to the CCS where IAV is internalized. (A and B) Typical confocal image sequences, visualized in a slice 1 μm above the glass surface. The CME (square boxes) (A) and the CIE (square boxes) (B) of IAV can be distinguished by the formation of CCS (green) spots at the place where IAV (magenta) bound (CME of IAV). Images were taken every 1 s. (C) Effects of cholesterol depletion (Depl) (by MβCD treatment), followed by cholesterol replenishment (Repl), on the CME and CIE of IAV. The results were normalized to the CME of IAV in nontreated cells (Intact). Intact, 115 IAVs in 32 cells; Depl, 102 IAVs in 49 cells; Repl, 103 IAVs in 29 cells. (D) A typical tricolor confocal image sequence (typical among 72 IAV spots in 25 cells) showing that an SM-cholesterol domain became colocalized with a CCS bound by an IAV virion (indicated by arrowheads with corresponding colors). Images were obtained every 2 s. At time zero, a CCS was formed at the place where IAV was bound to the PM (the CCS seen at −14 s did not migrate to the IAV). The IAV-CCS complex and the OlyA-bound SM-cholesterol domain exhibited slow diffusion-like behaviors (~0 to 70 s), collided with each other at 70 s, and became colocalized at 80 s. At 100 s, the CCS was disintegrated; at 120 s, IAV (probably in an early endosome) moved away from the observation plane (1 μm above the glass); and the OlyA-bound SM-cholesterol domain kept diffusing in the PM. (E) Fractions of the IAV-clathrin complex spots colocalized with the OlyA-bound SM-cholesterol domain before IAV internalization, evaluated by overlaying the IAV-clathrin images with the images of lipid probes correctly (Correct) and the doubly flipped (180°-rotated) images of lipid probes (Flip) (control), respectively.

65% ± 3% of the IAV particles in CCSs before internalization (74% ± 2% for colocalizations in the images overlaid correctly, minus 9% ± 1% for the incidental colocalizations found in the overlay of the 180°-rotated images of OlyA). The D4 spots (accessible cholesterol pool) were colocalized with only 6% ± 6% of the IAV particles in CCSs before internalization (Fig. 2E). These results strongly indicated that the SM-cholesterol complex, rather than the accessible cholesterol pool, is involved in the CME of IAV.

CME of IAV requires the SM-cholesterol complex nanodomains. We quantitatively examined how the internalized amounts of IAV were affected by the overexpression of the C-terminal domain of clathrin assembly protein 180 (AP180C) (AP180C fused to AcGFP1 at the N terminus of AP180C [GFP-AP180C]), which is known to specifically block CME without affecting CIE (33). Indeed, the overexpression of GFP-AP180C almost totally blocked Tf endocytosis, which occurs exclusively by CME (34) (Fig. 3A and D, left).

In the cells overexpressing GFP-AP180C, IAV internalization was reduced to 24% ± 4% of that in the intact cells (Fig. 3B, left, and Fig. 3D, IAV), indicating that 76% and 24% of IAV internalization occur by CME and CIE, respectively, consistent with the results shown in Fig. 2C. Interestingly, IAV internalization in cells after SMase or MβCD treatment for 60 min was reduced to levels very similar to those in AP180C-overexpressing cells (Fig. 1D and E and Fig. 3D, IAV). The results after the 30-min treatments are quite similar, as shown in Fig. S5A and B, and thus, the toxicity of these treatments for 60 min is limited, indicating that these 60-min treatments virtually blocked the CME

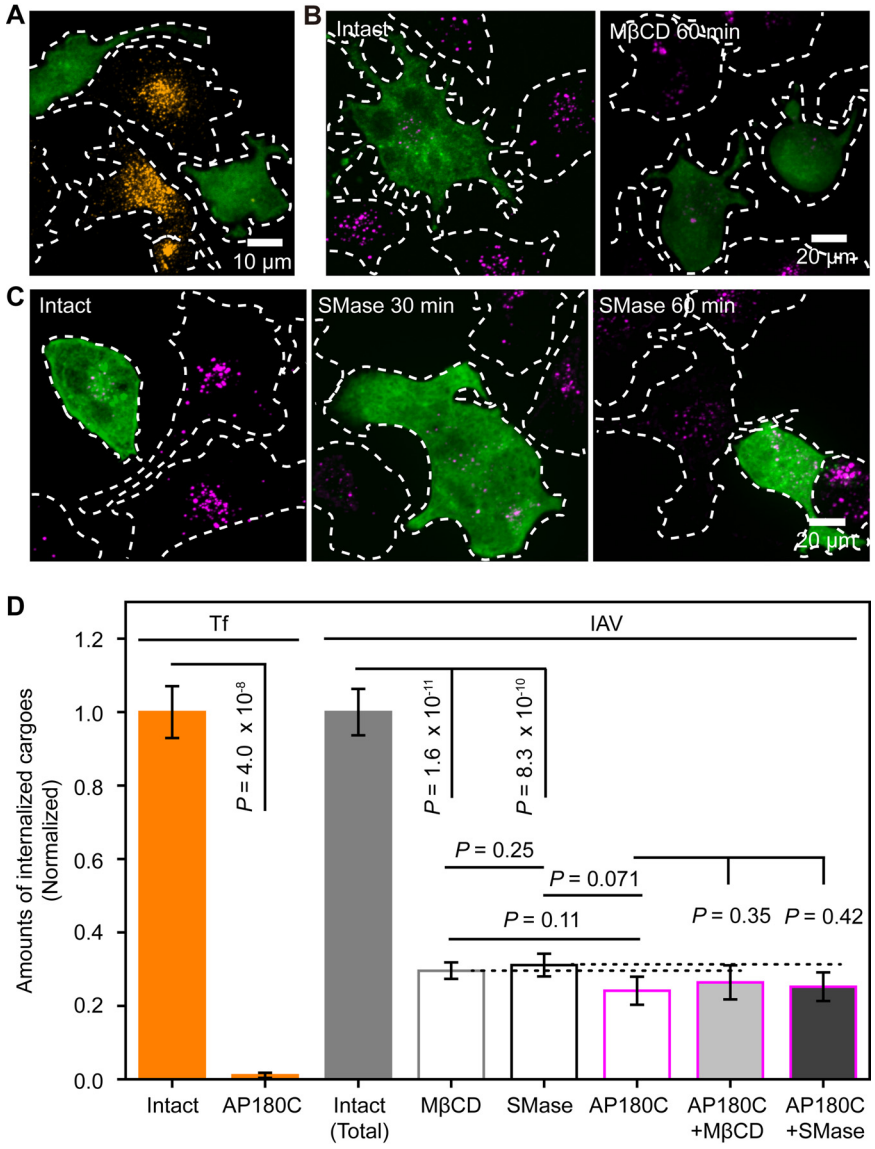

FIG 3 Depletion of SM-sequestered cholesterol blocked CME of IAV but not its CIE. (A) Typical image (among 12 images) showing that the cells expressing GFP-AP180C (green) hardly internalized Tf (orange), whereas those that did not express GFP-AP180C internalized Tf (basic data for panel D). (B, left) MDCK cells expressing GFP-AP180C (green) internalized much less IAV (magenta) than those that did not express GFP-AP180C (among 42 images). (Right) MβCD treatment reduced IAV internalization in MDCK cells that do not express GFP-AP180C, but it did not significantly affect the already-low IAV internalization in MDCK cells expressing GFP-AP180C (among 46 images). (C) Representative images showing the time course (0, 30, and 60 min)-dependent effects of SMase pretreatment on the amounts of internalized IAV (magenta), in cells with or without the expression of GFP-AP180C (green). The SMase pretreatment exhibited no apparent effect on IAV internalization in cells expressing GFP-AP180C but greatly suppressed IAV internalization in cells that do not express GFP-AP180C (see panel D; see also Fig. S5B in the supplemental material). (D) Amounts of internalized IAV and Tf after treating wild-type (WT) and AP180C-expressing cells with MβCD and SMase for 60 min, respectively. The amounts of internalized IAV and Tf were normalized to the amounts in the intact cell. GFP-AP180C expression almost totally (>99%) blocked the CME of Tf (orange bars), whereas it reduced IAV internalization by 74%, showing that ~26% of IAV internalization occurred by way of CIE (gray and magenta open bars). MβCD and SMase treatments reduced IAV internalization in cells without AP180C expression (gray and black open bars) but not that in cells overexpressing AP180C (magenta bar and light and dark gray bars with magenta borders), showing that the CIE of IAV depended on neither the accessible nor the SM-sequestered cholesterol pools.

of IAV. Moreover, the SMase treatment (which affects only SM-sequestered cholesterol) decreased IAV internalization as much as the MβCD treatment (which reduces both accessible and SM-sequestered cholesterol). These results suggested that the CME of IAV requires the SM-cholesterol complex but not the accessible cholesterol pool.

This hypothesis is supported by the following findings. The MβCD treatment and the SMase treatment of AP180C-expressing cells did not further reduce the amounts of internalized IAV (Fig. 3B, right, and Fig. 3C and D, IAV), indicating that the CIE of IAV does not require SM-sequestered cholesterol pools, consistent with the results obtained by single-virus tracking (Fig. 2). In addition, IAV internalization was not decreased in cells cultured with 50 μM mevalonate and 50 μM compactin (Fig. S5C), which would deplete accessible cholesterol but not SM-sequestered cholesterol (20). These results supported the proposals that the SM-cholesterol complex is required only for the CME of IAV and that the accessible cholesterol pool is dispensable for IAV internalization. Meanwhile, the addition of wortmannin, an inhibitor of macropinocytosis by blocking phosphatidylinositol 3-kinase, further reduced IAV internalization in AP180C-expressing cells (Fig. S5D to F), supporting the continued CIE of IAV in AP180C-expressing cells.

The SM-sequestered cholesterol pool is involved in all CME of IAV. The amounts of IAV and Tf internalized by way of CME were plotted against the total intensities of D4 (Fig. 4A and Fig. S6A) and OlyA (Fig. 4B and Fig. S6B). The amounts of D4 bound to the PM did not exhibit any simple correlation with the CME of either IAV or Tf (Fig. 4A). The wiggly correlations depended on the cholesterol depletion methods (Fig. 4A).

The CME of IAV (magenta) correlated monotonically with OlyA binding, without any clear dependence on the cholesterol depletion methods (Fig. 4B). Meanwhile, the amounts of internalized Tf against OlyA binding (via CME, no CIE) (orange) clearly depended on the cholesterol modulation methods, following two linear functions with different slopes (Fig. 4B, blue and green lines). This finding is consistent with the results shown in Fig. 3D (two bars from the right), indicating that a fraction of the CME of Tf depends on accessible cholesterol (since SMase treatment does not affect this pool).

Since the SM-sequestered and accessible cholesterol pools are substantially depleted after the 60-min treatments, the results after these treatments would provide a good estimation of the fractions sensitive to these two cholesterol pools (Fig. 4C). The results after the 30-min treatments were quite similar and are shown in Fig. S6C (for details of the calculations, see the Fig. 6C legend and Materials and Methods). We found that nearly all of the CME of IAV ($\sim$92%) requires SM-sequestered cholesterol, whereas the depletion of SM-sequestered cholesterol reduced Tf internalization by $\sim$50% (Fig. 4B), suggesting that in the case of Tf, SM-sequestered cholesterol is not essential but enhances the rate of Tf internalization by a factor of $\sim$2.

IAV internalization is enhanced in hypotonic medium only in the presence of the SM-cholesterol domain. The SM-cholesterol domain has higher bending rigidity, which might facilitate successful vesicle budding at high membrane tension (35, 36). Indeed, IAV internalization was greatly increased in hypotonic medium, which could increase the membrane tension of PM (Fig. 4D and Fig. S7A). This enhancement did not occur after SMase treatment (Fig. 4D and Fig. S7A). Meanwhile, Tf internalization was unaffected in hypotonic medium (Fig. 4D and Fig. S7B), consistent with a previous report (37). The SM-cholesterol domain is critical for the enhancement of IAV internalization in hypotonic medium, perhaps because it assists in the recruitment of actin, which was known to counteract increased membrane tension (37) or other unknown machineries.

The SM-cholesterol complex domain is required in the pit closure for IAV internalization. Neither MβCD treatment nor SMase treatment affected the number density and spatial distribution of CCSs on the PM, as found in both live and fixed cells (Fig. S8A and B). Furthermore, the lifetime of the CCSs on the PM became longer after the MβCD and SMase treatments (Fig. S8C), suggesting that the formation and maturation of CCSs were slower, in agreement with previous results (10, 11, 13).

To gain more insights into the stage(s) in the CME of IAV that requires the SM-cholesterol complex nanodomain, we observed the ultrafine shapes of CCSs by transmission electron microscopy (TEM). As shown in Fig. 5A, the CCS shapes, either with or without an IAV virion, were classified into four types, consistent with previous reports (37, 38): plate shape (flat to shallow-invagination type) (stage 1), U shape (deeply invaginated bowl type without constriction at the opening) (stage 2), Ω shape (deeply

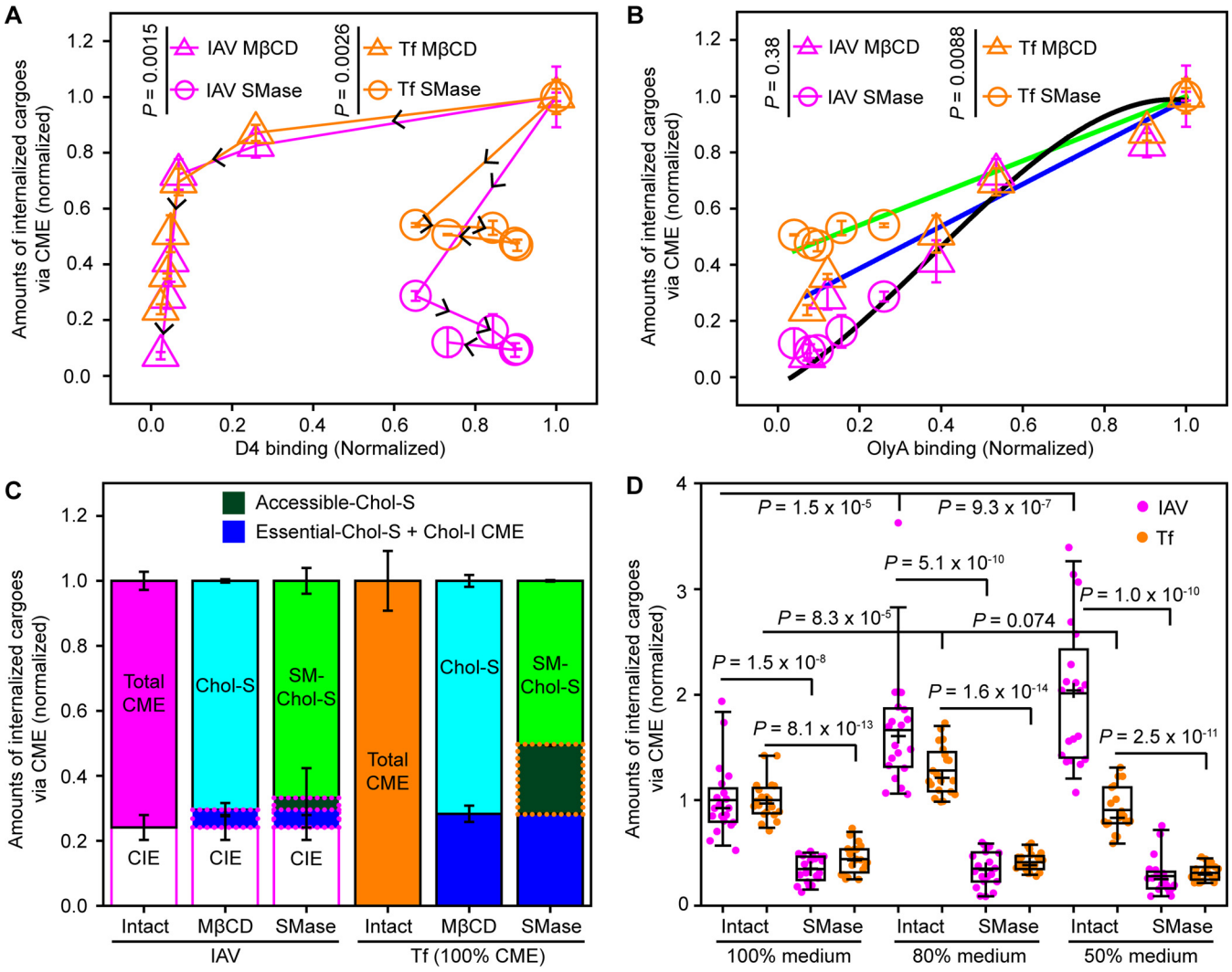

FIG 4 The CME of IAV depended on SM-sequestered cholesterol more than the CME of Tf. (A) The amounts of internalized IAV and Tf via CME are not simply related to the amounts of accessible cholesterol, as measured by mGFP-D4 binding. For the raw data, see Fig. 1C and E and Fig. S6 in the supplemental material. (B) The amounts of internalized IAV and Tf via CME monotonically decreased with decreasing amounts of SM-sequestered cholesterol, as measured by OlyA-mGFP binding. IAV internalization via CME depended on the amounts of SM-sequestered cholesterol in a manner independent of the cholesterol depletion methods (MβCD and SMase treatments) (the black cubic function is to facilitate visualization). Meanwhile, the CME of Tf depended not only on the amounts of SM-sequestered cholesterol but also on the methods of cholesterol depletion, suggesting that it depends on the accessible and essential cholesterol pools (green and blue straight lines). (C) Fractions of IAV and Tf internalized via CME with dependences on the three cholesterol pools. MβCD and SMase treatments were performed for 60 min. Chol, cholesterol; S, sensitive; I, insensitive. The fraction of CIE was taken from the sixth bar from the left in Fig. 3D (Tf internalization via CME is assumed to be 100%). Direct experimental and calculated results are indicated by the solid and dotted lines enclosing parts of the bars, respectively. The difference between the fraction sensitive to the MβCD treatment (cyan) and that sensitive to the SMase treatment (light green) gives an estimate for the fraction sensitive to only the accessible cholesterol pool (dark green bars). The fractions sensitive to essential cholesterol and cholesterol-insensitive CME (dark blue bars) were calculated by subtracting the fractions of SM-sequestered cholesterol (light green) and accessible cholesterol (dark green) from the fraction of CME (orange open bar). (D) Increased membrane tension by using diluted medium enhanced IAV internalization but not Tf internalization. The requirement of SM-sequestered cholesterol for IAV internalization remained the same. Horizontal bars, crosses, boxes, and whiskers indicate the median values, mean values, interquartile ranges (25 to 75%), and 10 to 90% ranges, respectively.

invaginated wineskin type with constriction) (stage 3), and vesicle shape (clathrin-coated vesicles) (stage 4).

Next, we quantified the CCSs in these four stages and examined the changes after MβCD treatment (Fig. 5B, left, and Fig. 5C, left), which depletes both the accessible and SM-sequestered cholesterol pools. But as described above (Fig. 3D and Fig. 4C), for the CME of IAV, only the SM-cholesterol complex is needed. After the MβCD treatment, the fraction of the CCSs containing an IAV virion at stage 1 remained the same, and that at stage 2 was significantly increased. However, the CCSs without an IAV virion, which would be the case for the CME of Tf, accumulated at stage 1 (the results with an

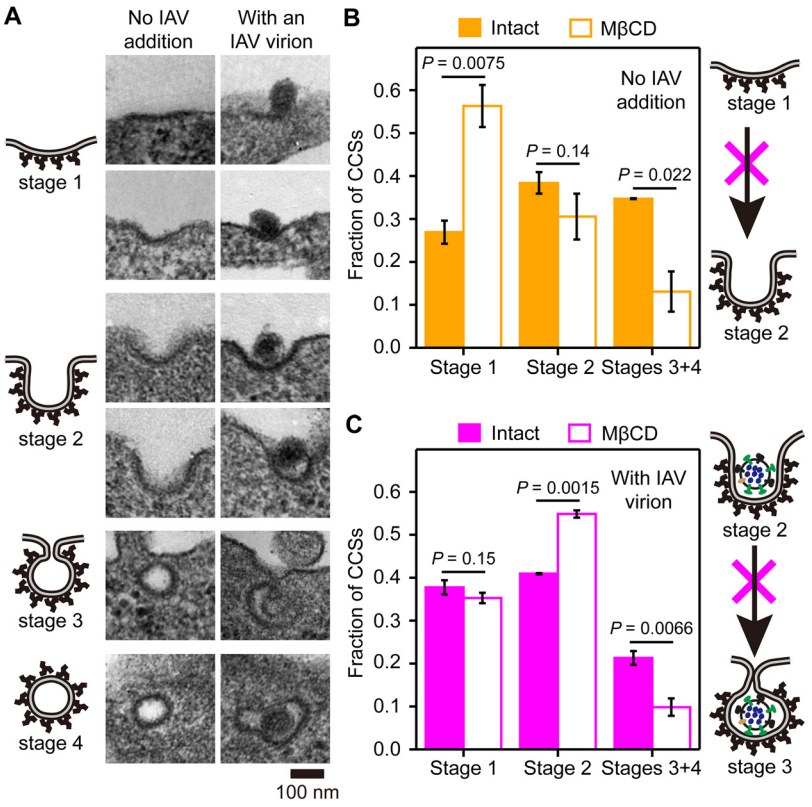

FIG 5 SM-cholesterol complex domains are required for the constriction of the CCS bound by IAV. (A) Representative transmission electron micrographs of the CCSs. (Left) No IAV addition; (right) with the IAV virion. (B and C) Fractions of the CCSs at stages 1, 2, and 3 to 4 before and after cholesterol depletion using MβCD. (B) No IAV addition; (C) CCSs with an IAV virion. The numbers of CCSs observed were 166 and 134 (no IAV addition) and 66 and 57 (with an IAV virion) before and after cholesterol depletion, respectively. Cholesterol depletion (accessible and/or SM-sequestered cholesterol) slowed the invagination of CCSs without any IAV virion, inducing an increase of the CCSs in stage 1 (plate type), with a concomitant decrease of the CCSs in stages 3 and 4 (bowl and vesicle types). With the binding of an IAV virion, even under cholesterol-depleted conditions, the transition from stage 1 to stage 2 occurred at a normal rate (no increase of the CCSs in stage 1). However, the cholesterol domain was required for the transition from stage 2 to stage 3.

IAV virion were obtained 15 min after IAV addition). This result indicated that the initial invagination of the CCS (for normal cargoes without an IAV virion) from stage 1 to stage 2 (from the plate shape to the bowl shape) is generally facilitated by accessible and/or SM-sequestered cholesterol (Fig. 5B, right). Meanwhile, the facilitation of the transitions from stage 1 to stage 2 by these cholesterol domains would not be necessary in the CCSs containing an IAV particle, probably because the invagination is facilitated by the multiple binding of IAV to many host membrane receptor molecules, inducing the indented negative curvature of the PM, consistent with previous proposals (4, 8, 39).

Meanwhile, MβCD treatment blocked the shape transition of the CCSs with an IAV virion from stage 2 (U shape) to stages 3 to 4 (Ω shape and vesicles) (Fig. 5C, left), consistent with fluorescence observations showing the considerable reduction of the CME of IAV after the MβCD treatment (Fig. 2C). This result strongly suggested that the SM-cholesterol complex in the CCS is required for neck constriction and pit closure rather than the initial invagination of the pit (Fig. 5C, right). In summary, in the absence of an IAV virion, as in the case of the CME of Tf, the accessible and SM-sequestered cholesterol pools are required for the initial invagination, whereas in the case of the CME of IAV, the SM-cholesterol complex nanodomain is required for inducing constriction at the neck of the CCS.

The recruitment of membrane-bending proteins FBP17, CIP4, pacsin2, and EndoA2 to the CCS depends on the SM-cholesterol complex. Our electron microscopy (EM) data indicated that the SM-cholesterol complex assists in the neck constriction of the IAV-containing CCP (Fig. 5). Thus, we hypothesized that the SM-cholesterol complex might recruit some of the key membrane-bending proteins for the CME of IAV.

First, using confocal microscopy, we examined the cholesterol dependence of the recruitment of seven ubiquitously expressed membrane-bending proteins (40, 41), Epsin1, F-BAR domain-only protein 2 (FCHo2), FBP17, N-terminal Fer/Cdc42-interacting protein 4 (CIP4), protein kinase C and casein kinase substrate in neurons protein 2 (pacsin2), endophilinA2 (EndoA2), and sorting nexin 9 (SNX9) (Fig. 6). Epsin1 and FCHo2 were extensively colocalized with the CCSs, but others exhibited much less colocalization with the CCSs (Fig. 6). The recruitment of Epsin1 and FCHo2 exhibited no cholesterol dependence, whereas cholesterol depletion increased the recruitment of SNX9. The proteins that exhibited decreased recruitment after cholesterol depletion were FBP17, CIP4, pacsin2, and EndoA2 (Fig. 6 and Fig. S9A), which are of interest to this study.

Among these four proteins, we further examined FBP17 and pacsin2. Since EndoA2 was known to be recruited to the CCS immediately before the scission of the CCP from the PM, and since our EM study found that IAV entry after cholesterol depletion stalls at the neck constriction stage, we did not investigate the involvement of EndoA2 any further (40, 42). Since FBP17 and CIP4 belong to the same transducer of Cdc42-dependent actin assembly (TOCA) protein family (43), we did not examine the recruitment of CIP4 any further.

The SM-cholesterol complex nanodomain recruits formin-binding protein FBP17 to the IAV-containing CCS. Using single-virus tracking with visualization of the clusters of pacsin2 and FBP17 (only clusters/oligomers are detectable with the present confocal microscopy methods), we identified the colocalizations of IAV particles and these proteins (Fig. 7A). In intact cells without cholesterol depletion, 71% $\pm$ 7% of the internalized IAV became colocalized with FBP17 before cell entry of IAV, whereas only 15% $\pm$ 1% of the internalized IAV became colocalized with pacsin2 before cell entry of IAV (Fig. 7B). These results suggested that FBP17 but not pacsin2 is involved in IAV cell entry. Noting that $\sim$75% of IAV internalization occurs via CME (Fig. 3D), the results obtained for FBP17 here therefore suggested that FBP17 was recruited to virtually all the IAV that was endocytosed via CME. Consistent with these results, we found that FBP17 became colocalized with 88% $\pm$ 2% of the IAV internalized by CME but not the IAV internalized by CIE using three-color observations of single virus particles (labeled by ATTO647N), CCSs (marked by mScarlet-I-CLCa), and FBP17 (mEGFP-FBP17) in live cells (Fig. 7A, Fig. S9B, and Movie S4).

After cholesterol depletion with MβCD for 30 min, the fraction of internalized IAV that became colocalized with FBP17 before cell entry was reduced to 40% $\pm$ 11% of that in the intact cell (Fig. 7B). The same MβCD treatment reduced the CME of IAV to 37% $\pm$ 7% (Fig. 3C). This agreement of the reduction extents by MβCD treatment strongly suggested that SM-cholesterol complex-dependent FBP17 recruitment to the CCS is required for CME of IAV.

The depletion of FBP17 from the cell using FBP17-specific small interference RNA (siRNA) (Fig. 7C) reduced IAV internalization to 64% $\pm$ 3% of that in control siRNA-transfected cells. The decrease of IAV internalization was less than 75% (Fig. 7D and E), perhaps due to redundant functions of curvature-driving proteins that could activate actin assembly at the endocytic site. These results suggested that the SM-cholesterol complex nanodomains in the IAV-containing CCS aid in the recruitment of FBP17, assisting in the CME of IAV (Fig. 7F).

DISCUSSION

Cholesterol homeostasis in the PM is known to affect many fundamental cellular functions, including pathogen infection (44, 45). In the present study, we found that SM-sequestered cholesterol, but not accessible or essential cholesterol, is essential for the CME of IAV (Fig. 1 and Fig. 4C). In contrast, the CME of Tf depends on any of the

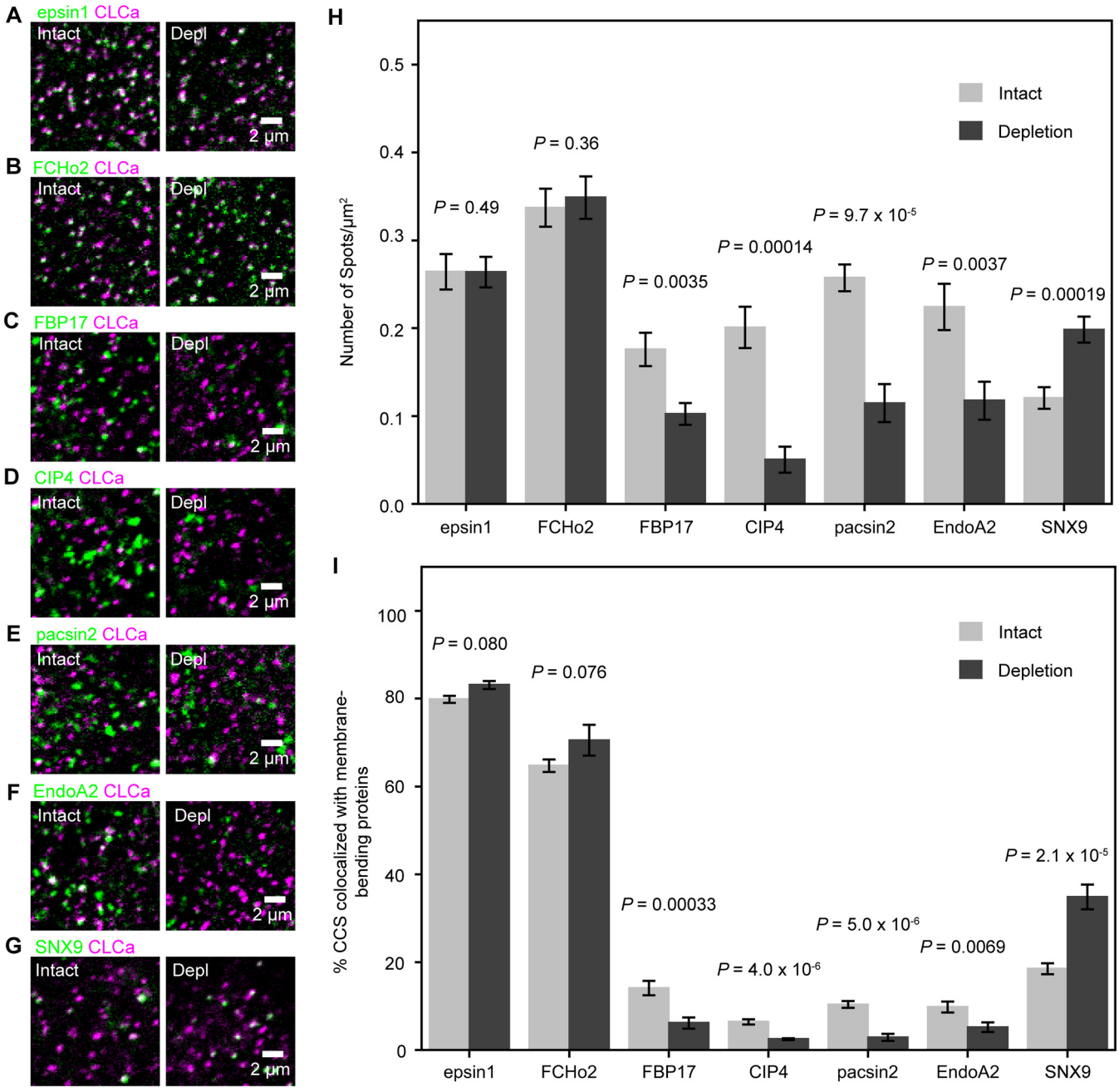

FIG 6 The recruitment of membrane-bending proteins to the CCS required SM-cholesterol complex domains. (A to G) Typical confocal images of the basal PM used for testing the colocalization of membrane-bending proteins (Epsin1, FCHo2, FBP17, CIP4, pacsin2, EndoA2, and SNX9) with the CCS before (intact) and after (Depl) SM-cholesterol complex depletion in live cells with MβCD for 30 min. Epsin1, 9 cells (intact and depletion); FCHo2, 10 cells (intact) and 11 cells (depletion); FBP17, 17 cells (intact) and 11 cells (depletion); CIP4, 16 cells (intact) and 17 cells (depletion); EndoA2, 11 cells (intact) and 8 cells (depletion); pacsin2, 10 cells (intact) and 7 cells (depletion); SNX9, 18 cells (intact) and 14 cells (depletion). (H and I) Number densities of fluorescent spots of membrane-bending proteins (H) and fractions of the CCS colocalized by the fluorescent spots of membrane-bending proteins (I) on the basal PM and the dorsal PM at a height of ~1 μm from the basal PM before and after cholesterol depletion.

three cholesterol pools (Fig. 4C), clearly showing that the molecular mechanisms and dynamics (see Fig. S10 in the supplemental material) involved in the CME of different cargoes are remarkably heterogeneous (14, 46). Furthermore, we found that the CIE of IAV (~24% of total IAV internalization) is cholesterol independent (Fig. 2C and Fig. 3D). These results indicated that, as in signaling (26) and immune reactions (27, 28), each endocytic pathway and cargo requires a pathway/cargo-specific cholesterol pool(s) for productive cell entry, thus providing new insights into the physiological functions of distinct cholesterol pools.

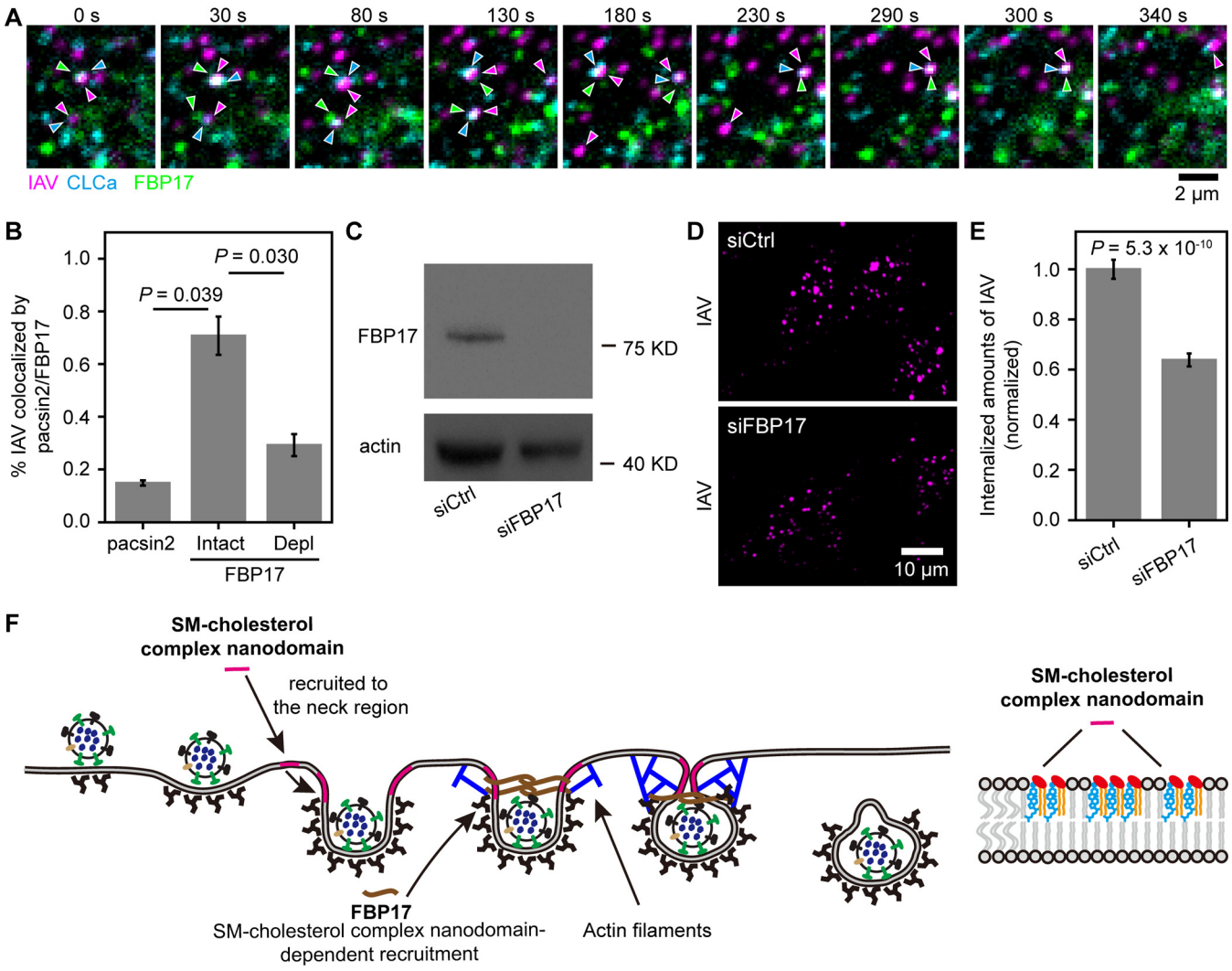

FIG 7 SM-sequestered cholesterol is required for the recruitment of FBP17 to the IAV-CCS complex during IAV entry. (A) A typical tricolor confocal image sequence showing that FBP17 became colocalized with a CCS bound by an IAV virion. Images were obtained every 2 s. Three typical events are shown in this image sequence. (B) SM-sequestered cholesterol is required for the recruitment of FBP17 in IAV cell entry, whereas pacsin2 is not involved in IAV cell entry. pacsin2, 65 IAVs in 20 cells; FBP17-Intact, 102 IAVs in 35 cells; FBP17-Depl, 78 IAVs in 42 cells. (C) Western blot pattern showing that transfection of an siRNA targeting FBP17 (siFBP17) reduced the expression of FBP17 by over 90%. siCtrl, control siRNA. (D) Representative confocal images of internalized IAV in cells without (among 24 cells) or after (among 30 images) FBP17 depletion showing that FBP17 is involved in IAV internalization. (E) Depletion of FBP17 reduced IAV internalization by ~40%. (F) Schematic model depicting the role of the SM-cholesterol complex nanodomain in CME of IAV. The SM-cholesterol complex nanodomain is recruited to the IAV-containing CCS. Due to the high bending rigidity of the SM-cholesterol nanodomain, when it is recruited to the neck region of the CCS, it could press the IAV-bound region of the CCS inward. The SM-cholesterol complex nanodomain is also essential for the recruitment of FBP17, a membrane-bending protein, which activates actin assembly, inducing the constriction of the IAV-containing CCP.

Our TEM results indicated that cholesterol aids in the invagination of the CCS without IAV from the plate stage to the bowl stage (Fig. 5B), whereas it helps in the closure of the opening of the IAV-containing CCS (Fig. 5C). These electron microscopy data, together with the fluorescence microscopy results, suggested that the SM-cholesterol complex nanodomain is recruited to the IAV-containing CCS (Fig. 2D and E and Fig. S4G) and aids in the neck constriction of the CCS containing an IAV virion. We propose that the SM-cholesterol complex nanodomain facilitates the formation of the CCS neck region. This might occur because the SM-cholesterol complex domain, with its higher bending rigidity, could press the IAV-bound part of the CCS inward, consistent with our finding that the increased membrane tension in the presence of the SM-sequestered cholesterol pool enhanced IAV internalization (Fig. 4D).

Using confocal microscopy, we found that the recruitment of Epsin1, a cargo-specific adaptor for the CME of IAV (47), exhibited no cholesterol dependence (Fig. 6). This

result is consistent with the electron microscopy results, suggesting that the early stages of IAV internalization via the CME were not affected by the SM-cholesterol complex. Furthermore, we found that the SM-cholesterol complex in the IAV-containing CCS plays a critical role in enhancing neck constriction by recruiting the membrane-bending protein FBP17, which is quite essential for CME of IAV (Fig. 7 and Fig. S7D). The recruited FBP17 would induce neck closure by activating actin assembly (37, 48, 49). Constriction by the actin filaments would be necessary for overcoming high membrane tension in the neck region as well as for enhancing scission (37, 49).

For the internalizations of various virus particles that are much larger than Tf (4), the involvements of actin filaments (50, 51) and microtubule-dependent LY6E tubules (52) have been reported. Here, we found the requirement of the SM-sequestered cholesterol pool for CME of IAV due to its role in recruiting FBP17 to the IAV-containing CCS. Understanding the relationships of these processes for the internalization of particles with various sizes and shapes will be an important target in future studies.

MATERIALS AND METHODS

Cell culture. MDCK cells (from the Center for Disease Control and Prevention, Hubei Province, China) were cultured in Dulbecco's minimum essential medium (DMEM; Thermo Scientific) supplemented with 5% fetal bovine serum (FBS; PAN-Biotech). HeLa cells (ATCC CCL-2) were grown in Eagle's minimum essential medium (MEM; GE Healthcare) supplemented with 10% FBS. All cell lines were tested with a GMyc-PCR mycoplasma test kit (Yeasen) and found to be mycoplasma-free.

Quantification of IAV and Tf internalizations. The IAV strains A/Puerto Rico/8/1934 (H1N1) (PR8) and A/Hubei/01-MA01/1999 (H9N2) were amplified in 10-day-old specific-pathogen-free (SPF) embryonated eggs (Merial China). IAV was tagged with sulfo-NHS-SS-biotin (Thermo Scientific) essentially as described previously (53, 54). IAV labeled with sulfo-NHS-SS-biotin was added to the cells; the mixture was incubated at 4°C for 15 min for adsorption on the PM outer surface; and after three washes with phosphate-buffered saline (PBS) precooled to 0°C, the cells were warmed to 37°C and incubated for 30 min. To remove the biotin probes on the IAV virions remaining on the cell surface, after a wash with ice-cold PBS, the cells were incubated in ice-cold Tris saline (50 mM Tris-HCl, 100 mM NaCl, 1 mM $MgCl_2$, 1 mM $CaCl_2$ [pH 8.6]) containing 100 mM 2-mercaptoethanesulfonate (MESNA; Maya Reagents) on ice for 30 min. Internalized IAV virions still tagged with biotin were stained with Cy3-labeled streptavidin (Cy3-SA; Thermo Scientific) after fixation with 4% (wt/vol) paraformaldehyde at room temperature for 30 min, followed by permeabilization with PBS containing 0.1% Triton X-100. Finally, the labeled cells were observed by spinning confocal fluorescence microscopy.

For quantifying Tf internalization, tetramethylrhodamine-conjugated Tf (TMR-Tf; Thermo Scientific) was added to the cells at a final concentration of 25 ng $\cdot$ mL^{-1} in serum-free culture medium, and the mixture was incubated at 37°C under a 5% CO_2 atmosphere for 10 min. The cells were placed on ice and washed with ice-cold buffer (pH 2.5) (100 mM glycine, 150 mM NaCl) to remove TMR-Tf bound on the cell surface. After fixation with 4% (wt/vol) paraformaldehyde at room temperature for 30 min, the cells were then imaged by confocal fluorescence microscopy. The maximum-intensity projections of the three-dimensional (3D) confocal image slices are shown in this report unless otherwise specified, and they were always used for quantifying the confocal imaging results.

Plasmid preparation and transfection. The EGFP sequences in the pEGFP-C1 and pEGFP-N1 plasmid vectors (Clontech) were replaced by mEGFP(A206K), a monomeric mutant of EGFP, or mScarlet-I, a red fluorescent protein (55). All primers were purchased from Sangon Biotech (see Table S1 in the supplemental material). The cDNA sequences encoding CLCa, Epsin1, FCHo2, FBP17, CIP4, pacsin2, EndoA2, and SNX9 were amplified from in-house cDNA libraries of MDCK cells and HeLa cells by PCR. AcGFP1-AP180C was prepared as described in our previous report (3).

The cells were transfected with selected plasmids using Lipofectamine 3000 (Thermo Scientific), according to the manufacturer's instructions. Transfected cells were reseeded onto glass-bottom dishes (In Vitro Scientific) 24 h before microscopic observations.

Cholesterol depletion and replenishment. To lower the cholesterol content in the cell, and particularly in the PM, the cells were incubated with 10 mM MβCD (Sigma-Aldrich) in serum-free culture medium at 37°C under a 5% CO_2 atmosphere for the selected durations. To restore the cholesterol, the cells were incubated with cholesterol complexed with MβCD (Sigma-Aldrich) at 37°C under a 5% CO_2 atmosphere for 30 min.

The cholesterol content of the entire cell was evaluated in the following way. First, the total lipid from the entire cell was extracted with a mixture of chloroform, isopropanol, and NP-40 (7:11:0.1 [by volume]) and dried under a vacuum. The amount of cholesterol in the extracted lipids was measured with an AAT-Bioquest cholesterol quantitation kit based on the enzymatic activity of cholesterol oxidase, according to the manufacturer's instructions. The fluorescence at 590 nm was measured with a BioTek plate reader.

To selectively deplete accessible cholesterol, MDCK cells were cultured in DMEM with 5% FBS for 12 h, followed by DMEM with 5% lipoprotein-deficient FBS with or without 50 μM sodium mevalonate and 50 μM compactin for 48 h (20).

SMase treatment and SM replenishment. SMase purified from *Staphylococcus* (Sigma-Aldrich) was diluted to 1.25 U/mL in serum-free DMEM on ice. The cells were incubated with the SMase-containing medium at 37°C under a 5% CO_2 atmosphere for 30 min and then washed three times with PBS. To replenish the SM, SM purified from chicken egg yolk (Sigma-Aldrich) and bovine serum albumin (BSA; Amresco) were mixed in DMEM at final concentrations of 30 mM and 0.3 mM, respectively. This solution was added to the cells at 37°C under a 5% CO_2 atmosphere for 30 min, followed by three washes with PBS.

Production and purification of the recombinant protein biosensors for the accessible cholesterol pool (mEGFP-D4) and the SM-sequestered cholesterol pool (OlyA-mEGFP) in the PM and their binding to the cell surface. To produce mEGFP-labeled lipid-binding proteins, the open reading frames (ORFs) of mEGFP or mEGFP with a linker encoding the GGGS sequence at both the N and C termini (SG-mEGFP-SG) were amplified and inserted into the pET26b vector (Merck). The cDNAs encoding domain 4 of perfringolysin O (D4) with the single mutation D495S (56) and OlyA were chemically synthesized by Sangon Biotech, and their sequences were confirmed in our laboratory. These cDNAs were inserted into the pET26b-mEGFP vector for the expression of mEGFP-D4-His and OlyA-SG-mEGFP-SG-His. These proteins were expressed in *Escherichia coli* BL21(DE3) and isolated, basically according to a previously reported protocol (57). Briefly, the bacteria were cultured at 37°C in Luria-Bertani (LB) medium containing 50 μg/mL kanamycin, with agitation, until the optical density at 600 nm reached 0.4 to 0.6. The suspension was cooled to room temperature, isopropyl-β-D-thiogalactopyranoside (IPTG; Amresco) was then added to the suspension at a final concentration of 0.6 mM, and the cells were cultured with agitation at 25°C for 12 h. The cells were collected by centrifugation at 5,000 rpm for 5 min. The pellet was resuspended in lysis buffer (Sangon Biotech) and disrupted by sonication for 20 min. The suspension was centrifuged at 12,000 rpm for 10 min, and the supernatant was again centrifuged at the same speed for 10 min to further remove the cell debris. The recombinant proteins in the supernatant were purified by nitrilotriacetic acid (NTA)-Ni column chromatography (Sangon Biotech).

Purified mEGFP-D4 and OlyA-mEGFP were added to cells cultured in glass-bottom dishes at a final concentration of 1 μM at 37°C for 15 min. After washing with PBS three times, the OlyA-mEGFP and mEGFP-D4 bound to the cells were examined with a spinning confocal fluorescence microscope.

Immunofluorescence. Rabbit polyclonal antibodies against the clathrin light chain were obtained from Proteintech, the mouse monoclonal antibody against hemagglutinin of H9N2 was obtained from Sino Biological, and the DyLight 488- and 647-labeled secondary antibodies were obtained from Abbkine. Cells cultured in glass-bottom dishes were fixed with 4% (wt/vol) paraformaldehyde at room temperature for 20 min and then permeabilized and blocked in QuickBlock buffer (Beyotime) with 0.1% Triton X-100 for 15 min. Specimens were incubated with primary antibodies in QuickBlock buffer (1:400) at 37°C for 90 min, followed by incubation with DyLight 649-conjugated secondary antibodies in QuickBlock buffer (1:400) at 37°C for 45 min.

Confocal fluorescence microscopy imaging. All confocal fluorescence microscopic observations were performed with a Perkin-Elmer UltraVIEW Vox confocal imaging system built on a Nikon Ti-E inverted microscope equipped with a piezo stage (Prior Scientific), an autofocus system (Nikon), and a 100× lens objective (Nikon Plan Apochromat, 1.40 numerical aperture [NA]). For single-IAV-virion tracking on live cells, cells were observed in PBS supplemented with 1 mM Ca^{2+}, 0.5 mM Mg^{2+}, 0.1% BSA, and 5 mM glucose (PBS^{++}) at 37°C in a temperature-controlled incubator (Tokai Hit INUB-PPZI2-F1).

For image-based quantification of internalized cargoes, the fixed cells were observed in PBS with a 60× lens objective (Nikon Plan Apochromat, 1.40 NA). Quantification of the 3D images was performed using the 3D Objects Counter plug-in of Fiji (NIH). The fractions of mScarlet-I-labeled CCSs colocalized with mEGFP-labeled membrane-bending proteins and indirect immunofluorescence (IF)-stained IAV (labeled with DyLight 488) with Cy3-SA-labeled IAV (by way of biotin and SA interactions) were quantified using the ComDet plug-in of Fiji (NIH). All tracking-based analyses were performed using u-track software (58) running on Matlab (MathWorks). The intensity and velocity of the visualized fluorescence spots were determined by custom-written software.

Calculation of the fractions of the cargoes internalized via different endocytic pathways. The internalized amounts of IAV and Tf were normalized to those in intact cells. Tf internalization occurs solely via CME (34). Meanwhile, IAV can be internalized by both CME and CIE. The CME of IAV is totally blocked in cells expressing AcGFP-AP180C (Fig. 3A and D), and thus, only CIE is active for IAV internalization in these cells. Furthermore, in these cells, IAV internalization was insensitive to MβCD and SMase treatments up to 60 min (Fig. 3D and Fig. S5B), showing that the CIE of IAV is independent of the accessible and SM-sequestered cholesterol pools. The fractions of CIE are taken from the results of the AP180C-expressing cells in Fig. S5B and Fig. 3D (the sixth bar from the left; the difference is shown in the orange open bars; no CIE for Tf is assumed).

MβCD treatment (partially) depletes both the accessible and SM-sequestered cholesterol pools, whereas SMase treatment (partially) depletes only SM-sequestered cholesterol. The depletion of the two cholesterol pools is more complete after the 60-min treatments (Fig. 3D); these results provided a better estimation of the fractions sensitive to these two pools of cholesterol. For details about the fractions of the internalized cargoes (IAV and Tf) and their calculations, see the legends of Fig. S6C and Fig. 4C, respectively.

RNA interference. HeLa cells were plated into 12-well plates and allowed to grow for 12 h. All siRNAs (80 nM; Sangon Biotech) were introduced into cells using 4 μL Lipofectamine 3000 (Thermo Scientific) twice according to the manufacturer's instructions. All experiments were performed 72 h after siRNA transfection. For imaging, cells were plated into glass-bottom dishes 24 h after the second transfection. The

following siRNA sequences were used: CCA ACC UGA ACG AAA UGA AUG AUU A for FBP17 and UUC UCC GAA CGU GUC ACG UTT for negative-control siRNA.

Western blotting. Lysates of cells were obtained by adding 100 μL of radioimmunoprecipitation assay (RIPA) lysis buffer (Yeasen) supplemented with a protease inhibitor cocktail and boiling with 5× SDS-PAGE sample loading buffer (Yeasen). Samples were resolved by SurePAGE (GenScript), transferred to a polyvinylidene difluoride (PVDF) membrane (Millipore), and blocked with QuickBlock buffer (Beyotime). FBP17 and actin were stained with anti-FBP17 (Santa Cruz) (1:100) and anti-beta-actin (Proteintech) (1:1,000) antibodies at room temperature for 2 h followed by horseradish peroxidase (HRP)-coupled secondary antibodies (Sangon) (1:10,000) at room temperature for 1 h. The protein bands were imaged using GelDoc XR (Bio-Rad).

Electron microscopy. The cells were fixed with 2.5% glutaraldehyde in PBS (pH 7.2) at 4°C for 4 h, washed with ice-cold PBS three times, and then scraped off the plates with a rubber policeman. The cells were collected by centrifugation, and the pellet was fixed using osmium tetroxide; dehydrated in ethanol, which was exchanged with acetone in graded concentrations of ethanol and acetone; and then embedded in epoxy resin. The embedded specimens were sectioned at thicknesses of 50 to 70 nm. The thin sections were stained with lead citrate. The samples were examined using a Philips CM 100 electron microscope at a ×50,000 magnification (75 kV).

Statistical analysis. All experimental results described here were obtained from at least two independent experiments. In each independent experiment, we measured at least three samples. The results of each independent experiment were normalized to the control group first, followed by the calculation of the standard error using normalized results from all independent experiments using Origin. Single-tail Student's *t* tests were performed to calculate the *P* values, using Excel. Multivariate analyses of variance (MANOVAs) were performed via a custom-written script in R.

Code availability. The code of the custom-written software is available from the corresponding author upon reasonable request.

Data availability. The data that support the findings of this study are available upon reasonable request.

SUPPLEMENTAL MATERIAL

Supplemental material is available online only.

SUPPLEMENTAL FILE 1, AVI file, 4.3 MB.

SUPPLEMENTAL FILE 2, AVI file, 5.9 MB.

SUPPLEMENTAL FILE 3, AVI file, 9.6 MB.

SUPPLEMENTAL FILE 4, AVI file, 14.8 MB.

SUPPLEMENTAL FILE 5, PDF file, 0.1 MB.

ACKNOWLEDGMENTS

The preparation of ultrathin sections was accomplished by the core facility center at the Wuhan Institute of Virology, Chinese Academy of Sciences. This work was supported by the National Key R&D Program of China (2019YFA0210100), the National Natural Science Foundation of China (91859123), and the Frontiers Science Center for New Organic Matter, Nankai University (63181206).

Bo Tang and Dai-Wen Pang conceived and formulated the project. Bo Tang performed virtually all the experiments. Bo Tang, En-Ze Sun, Zhi-Ling Zhang, and Dai-Wen Pang devised the method to quantify internalized IAV. Bo Tang, Shu-Lin Liu, and Dai-Wen Pang designed the assays based on single-virus tracking. Bo Tang, Akihiro Kusumi, and Dai-Wen Pang conceived D4- and OlyA-based assays. Bo Tang, Jia Liu, Zhi-Hong Hu, Tao Zeng, Ya-Feng Kang, and Hong-Wu Tang provided help in TEM observations and analysis. Bo Tang, Akihiro Kusumi, and Dai-Wen Pang wrote the manuscript. Dai-Wen Pang is the group leader to initiate the project. All authors discussed the results and participated in revising the manuscript.

REFERENCES

1. Lakadamyali M, Rust MJ, Babcock HP, Zhuang XW. 2003. Visualizing infection of individual influenza viruses. Proc Natl Acad Sci U S A 100:9280–9285. https://doi.org/10.1073/pnas.0832269100.
2. de Vries E, Tscherne DM, Wienholts MJ, Cobos-Jimenez V, Scholte F, Garcia-Sastre A, Rottier PJM, de Haan CAM. 2011. Dissection of the influenza A virus endocytic routes reveals macropinocytosis as an alternative entry pathway. PLoS Pathog 7:e1001329. https://doi.org/10.1371/journal.ppat.1001329.
3. Sun EZ, Liu AA, Zhang ZL, Liu SL, Tian ZQ, Pang DW. 2017. Real-time dissection of distinct dynamin-dependent endocytic routes of influenza A virus by quantum dot-based single-virus tracking. ACS Nano 11:4395–4406. https://doi.org/10.1021/acsnano.6b07853.
4. Mercer J, Schelhaas M, Helenius A. 2010. Virus entry by endocytosis. Annu Rev Biochem 79:803–833. https://doi.org/10.1146/annurev-biochem-060208-104626.
5. Ketter E, Randall G. 2019. Virus impact on lipids and membranes. Annu Rev Virol 6:319–340. https://doi.org/10.1146/annurev-virology-092818-015748.
6. Lakadamyali M, Rust MJ, Zhuang X. 2006. Ligands for clathrin-mediated endocytosis are differentially sorted into distinct populations of early endosomes. Cell 124:997–1009. https://doi.org/10.1016/j.cell.2005.12.038.

7. Miyake Y, Keusch JJ, Decamps L, Ho-Xuan H, Iketani S, Gut H, Kutay U, Helenius A, Yamauchi Y. 2019. Influenza virus uses transportin 1 for vRNP debundling during cell entry. Nat Microbiol 4:578–586. https://doi.org/10.1038/s41564-018-0332-2.
8. Sieben C, Sezgin E, Eggeling C, Manley S. 2020. Influenza A viruses use multivalent sialic acid clusters for cell binding and receptor activation. PLoS Pathog 16:e1008656. https://doi.org/10.1371/journal.ppat.1008656.
9. Baumgart T, Hess ST, Webb WW. 2003. Imaging coexisting fluid domains in biomembrane models coupling curvature and line tension. Nature 425:821–824. https://doi.org/10.1038/nature02013.
10. Rodal SK, Skretting G, Garred O, Vilhardt F, van Deurs B, Sandvig K. 1999. Extraction of cholesterol with methyl-β-cyclodextrin perturbs formation of clathrin-coated endocytic vesicles. Mol Biol Cell 10:961–974. https://doi.org/10.1091/mbc.10.4.961.
11. Subtil A, Gaidarov I, Kobylarz K, Lampson MA, Keen JH, McGraw TE. 1999. Acute cholesterol depletion inhibits clathrin-coated pit budding. Proc Natl Acad Sci U S A 96:6775–6780. https://doi.org/10.1073/pnas.96.12.6775.
12. Mayor S, Pagano RE. 2007. Pathways of clathrin-independent endocytosis. Nat Rev Mol Cell Biol 8:603–612. https://doi.org/10.1038/nrm2216.
13. Shen H, Giordano F, Wu Y, Chan J, Zhu C, Milosevic I, Wu X, Yao K, Chen B, Baumgart T, Sieburth D, De Camilli P. 2014. Coupling between endocytosis and sphingosine kinase 1 recruitment. Nat Cell Biol 16:652–662. https://doi.org/10.1038/ncb2987.
14. Mettlen M, Chen PH, Srinivasan S, Danuser G, Schmid SL. 2018. Regulation of clathrin-mediated endocytosis. Annu Rev Biochem 87:871–896. https://doi.org/10.1146/annurev-biochem-062917-012644.
15. Chu VC, Whittaker GR. 2004. Influenza virus entry and infection require host cell N-linked glycoprotein. Proc Natl Acad Sci U S A 101:18153–18158. https://doi.org/10.1073/pnas.0405172102.
16. Barman S, Nayak DP. 2007. Lipid raft disruption by cholesterol depletion enhances influenza A virus budding from MDCK cells. J Virol 81:12169–12178. https://doi.org/10.1128/JVI.00835-07.
17. Amini-Bavil-Olyaee S, Choi YJ, Lee JH, Shi M, Huang IC, Farzan M, Jung JU. 2013. The antiviral effector IFITM3 disrupts intracellular cholesterol homeostasis to block viral entry. Cell Host Microbe 13:452–464. https://doi.org/10.1016/j.chom.2013.03.006.
18. Bajimaya S, Frankl T, Hayashi T, Takimoto T. 2017. Cholesterol is required for stability and infectivity of influenza A and respiratory syncytial viruses. Virology 510:234–241. https://doi.org/10.1016/j.virol.2017.07.024.
19. Musiol A, Gran S, Ehrhardt C, Ludwig S, Grewal T, Gerke V, Rescher U. 2013. Annexin A6-balanced late endosomal cholesterol controls influenza A replication and propagation. mBio 4:e00608-13. https://doi.org/10.1128/mBio.00608-13.
20. Das A, Brown MS, Anderson DD, Goldstein JL, Radhakrishnan A. 2014. Three pools of plasma membrane cholesterol and their relation to cholesterol homeostasis. Elife 3:e02882. https://doi.org/10.7554/eLife.02882.
21. Das A, Goldstein JL, Anderson DD, Brown MS, Radhakrishnan A. 2013. Use of mutant I-125-perfringolysin O to probe transport and organization of cholesterol in membranes of animal cells. Proc Natl Acad Sci U S A 110:10580–10585. https://doi.org/10.1073/pnas.1309273110.
22. Ogasawara F, Kano F, Murata M, Kimura Y, Kioka N, Ueda K. 2019. Changes in the asymmetric distribution of cholesterol in the plasma membrane influence streptolysin O pore formation. Sci Rep 9:4548. https://doi.org/10.1038/s41598-019-39973-x.
23. Chakrabarti RS, Ingham SA, Kozlitina J, Gay A, Cohen JC, Radhakrishnan A, Hobbs HH. 2017. Variability of cholesterol accessibility in human red blood cells measured using a bacterial cholesterol-binding toxin. Elife 6:e23355. https://doi.org/10.7554/eLife.23355.
24. Skočaj M, Resnik N, Grundner M, Ota K, Rojko N, Hodnik V, Anderluh G, Sobota A, Maček P, Veranič P, Sepčić K. 2014. Tracking cholesterol/sphingomyelin-rich membrane domains with the ostreolysin A-mCherry protein. PLoS One 9:e92783. https://doi.org/10.1371/journal.pone.0092783.
25. Endapally S, Frias D, Grzemska M, Gay A, Tomchick DR, Radhakrishnan A. 2019. Molecular discrimination between two conformations of sphingomyelin in plasma membranes. Cell 176:1040–1053. https://doi.org/10.1016/j.cell.2018.12.042.
26. Kinnebrew M, Iverson EJ, Patel BB, Pusapati GV, Kong JH, Johnson KA, Luchetti G, Eckert KM, McDonald JG, Covey DF, Siebold C, Radhakrishnan A, Rohatgi R. 2019. Cholesterol accessibility at the ciliary membrane controls hedgehog signaling. Elife 8:e5005. https://doi.org/10.7554/eLife.50051.
27. Zhou QD, Chi X, Lee MS, Hsieh WY, Mkrtchyan JJ, Feng A-C, He C, York AG, Bui VL, Kronenberger EB, Ferrari A, Xiao X, Daly AE, Tarling EJ, Damoiseaux R, Scumpia PO, Smale ST, Williams KJ, Tontonoz P, Bensinger SJ. 2020. Interferon-mediated reprogramming of membrane cholesterol to evade bacterial toxins. Nat Immunol 21:746–755. https://doi.org/10.1038/s41590-020-0695-4.
28. Abrams ME, Johnson KA, Perelman SS, Zhang L, Endapally S, Mar KB, Thompson BM, McDonald JG, Schoggins JW, Radhakrishnan A, Alto NM. 2020. Oxysterols provide innate immunity to bacterial infection by mobilizing cell surface accessible cholesterol. Nat Microbiol 5:929–942. https://doi.org/10.1038/s41564-020-0701-5.
29. Zidovetzki R, Levitan I. 2007. Use of cyclodextrins to manipulate plasma membrane cholesterol content: evidence, misconceptions and control strategies. Biochim Biophys Acta 1768:1311–1324. https://doi.org/10.1016/j.bbamem.2007.03.026.
30. Makino A, Abe M, Ishitsuka R, Murate M, Kishimoto T, Sakai S, Hullin-Matsuda F, Shimada Y, Inaba T, Miyatake H, Tanaka H, Kurahashi A, Pack C-G, Kasai RS, Kubo S, Schieber NL, Dohmae N, Tochio N, Hagiwara K, Sasaki Y, Aida Y, Fujimori F, Kigawa T, Nishibori K, Parton RG, Kusumi A, Sako Y, Anderluh G, Yamashita M, Kobayashi T, Greimel P, Kobayashi T. 2017. A novel sphingomyelin/cholesterol domain-specific probe reveals the dynamics of the membrane domains during virus release and in Niemann-Pick type C. FASEB J 31:1301–1322. https://doi.org/10.1096/fj.201500075R.
31. Naito T, Ercan B, Krshnan L, Triebl A, Koh DHZ, Wei F-Y, Tomizawa K, Torta FT, Wenk MR, Saheki Y. 2019. Movement of accessible plasma membrane cholesterol by the GRAMD1 lipid transfer protein complex. Elife 8:e51401. https://doi.org/10.7554/eLife.51401.
32. Rossman JS, Leser GP, Lamb RA. 2012. Filamentous influenza virus enters cells via macropinocytosis. J Virol 86:10950–10960. https://doi.org/10.1128/JVI.05992-11.
33. Zhao XH, Greener T, Al-Hasani H, Cushman SW, Eisenberg E, Greene LE. 2001. Expression of auxilin or AP180 inhibits endocytosis by mislocalizing clathrin: evidence for formation of nascent pits containing AP1 or AP2 but not clathrin. J Cell Sci 114:353–365. https://doi.org/10.1242/jcs.114.2.353.
34. Hopkins CR, Trowbridge IS. 1983. Internalization and processing of transferrin and the transferrin receptor in human carcinoma A431 cells. J Cell Biol 97:508–521. https://doi.org/10.1083/jcb.97.2.508.
35. Chakraborty S, Doktorova M, Molugu TR, Heberle FA, Scott HL, Dzikovski B, Nagao M, Stingaciu L-R, Standaert RF, Barrera FN, Katsaras J, Khelashvili G, Brown MF, Ashkar R. 2020. How cholesterol stiffens unsaturated lipid membranes. Proc Natl Acad Sci U S A 117:21896–21905. https://doi.org/10.1073/pnas.2004807117.
36. Hassinger JE, Oster G, Drubin DG, Rangamani P. 2017. Design principles for robust vesiculation in clathrin-mediated endocytosis. Proc Natl Acad Sci U S A 114:E1118–E1127. https://doi.org/10.1073/pnas.1617705114.
37. Boulant S, Kural C, Zeeh J-C, Ubelmann F, Kirchhausen T. 2011. Actin dynamics counteract membrane tension during clathrin-mediated endocytosis. Nat Cell Biol 13:1124–1131. https://doi.org/10.1038/ncb2307.
38. Posor Y, Eichhorn-Gruenig M, Puchkov D, Schöneberg J, Ullrich A, Lampe A, Müller R, Zarbakhsh S, Gulluni F, Hirsch E, Krauss M, Schultz C, Schmoranzer J, Noé F, Haucke V. 2013. Spatiotemporal control of endocytosis by phosphatidylinositol-3,4-bisphosphate. Nature 499:233–237. https://doi.org/10.1038/nature12360.
39. Ewers H, Helenius A. 2011. Lipid-mediated endocytosis. Cold Spring Harb Perspect Biol 3:a004721. https://doi.org/10.1101/cshperspect.a004721.
40. Taylor MJ, Perrais D, Merrifield CJ. 2011. A high precision survey of the molecular dynamics of mammalian clathrin-mediated endocytosis. PLoS Biol 9:e1000604. https://doi.org/10.1371/journal.pbio.1000604.
41. Bhave M, Mino RE, Wang XX, Lee J, Grossman HM, Lakoduk AM, Danuser G, Schmid SL, Mettlen M. 2020. Functional characterization of 67 endocytic accessory proteins using multiparametric quantitative analysis of CCP dynamics. Proc Natl Acad Sci U S A 117:31591–31602. https://doi.org/10.1073/pnas.2020346117.
42. Daumke O, Roux A, Haucke V. 2014. BAR domain scaffolds in dynamin-mediated membrane fission. Cell 156:882–892. https://doi.org/10.1016/j.cell.2014.02.017.
43. Shimada A, Niwa H, Tsujita K, Suetsugu S, Nitta K, Hanawa-Suetsugu K, Akasaka R, Nishino Y, Toyama M, Chen LR, Liu ZJ, Wang BC, Yamamoto M, Terada T, Miyazawa A, Tanaka A, Sugano S, Shirouzu M, Nagayama K, Takenawa T, Yokoyama S. 2007. Curved EFC/F-BAR-domain dimers are joined end to end into a filament for membrane invagination in endocytosis. Cell 129:761–772. https://doi.org/10.1016/j.cell.2007.03.040.
44. Ikonen E. 2008. Cellular cholesterol trafficking and compartmentalization. Nat Rev Mol Cell Biol 9:125–138. https://doi.org/10.1038/nrm2336.
45. Ilnytska O, Santiana M, Hsu N-Y, Du W-L, Chen Y-H, Viktorova EG, Belov G, Brinker A, Storch J, Moore C, Dixon JL, Altan-Bonnet N. 2013.

Enteroviruses harness the cellular endocytic machinery to remodel the host cell cholesterol landscape for effective viral replication. Cell Host Microbe 14:281–293. https://doi.org/10.1016/j.chom.2013.08.002.
46. Loerke D, Mettlen M, Yarar D, Jaqaman K, Jaqaman H, Danuser G, Schmid SL. 2009. Cargo and dynamin regulate clathrin-coated pit maturation. PLoS Biol 7:e1000057. https://doi.org/10.1371/journal.pbio.1000057.
47. Chen C, Zhuang X. 2008. Epsin 1 is a cargo-specific adaptor for the clathrin-mediated endocytosis of the influenza virus. Proc Natl Acad Sci U S A 105:11790–11795. https://doi.org/10.1073/pnas.0803711105.
48. Takano K, Toyooka K, Suetsugu S. 2008. EFC/F-BAR proteins and the N-WASP-WIP complex induce membrane curvature-dependent actin polymerization. EMBO J 27:2817–2828. https://doi.org/10.1038/emboj.2008.216.
49. Tsujita K, Takenawa T, Itoh T. 2015. Feedback regulation between plasma membrane tension and membrane-bending proteins organizes cell polarity during leading edge formation. Nat Cell Biol 17:749–758. https://doi.org/10.1038/ncb3162.
50. Cureton DK, Massol RH, Saffarian S, Kirchhausen TL, Whelan SPJ. 2009. Vesicular stomatitis virus enters cells through vesicles incompletely coated with clathrin that depend upon actin for internalization. PLoS Pathog 5:e1000394. https://doi.org/10.1371/journal.ppat.1000394.
51. Cureton DK, Massol RH, Whelan SPJ, Kirchhausen T. 2010. The length of vesicular stomatitis virus particles dictates a need for actin assembly during clathrin-dependent endocytosis. PLoS Pathog 6:e1001127. https://doi.org/10.1371/journal.ppat.1001127.
52. Hackett BA, Cherry S. 2018. Flavivirus internalization is regulated by a size-dependent endocytic pathway. Proc Natl Acad Sci U S A 115:4246–4251. https://doi.org/10.1073/pnas.1720032115.
53. Liu SL, Tian ZQ, Zhang ZL, Wu QM, Zhao HS, Ren B, Pang DW. 2012. High-efficiency dual labeling of influenza virus for single-virus imaging. Biomaterials 33:7828–7833. https://doi.org/10.1016/j.biomaterials.2012.07.026.
54. Liu SL, Zhang ZL, Tian ZQ, Zhao H-S, Liu H, Sun EZ, Xiao GF, Zhang W, Wang HZ, Pang DW. 2012. Effectively and efficiently dissecting the infection of influenza virus by quantum-dot-based single-particle tracking. ACS Nano 6:141–150. https://doi.org/10.1021/nn2031353.
55. Bindels DS, Haarbosch L, van Weeren L, Postma M, Wiese KE, Mastop M, Aumonier S, Gotthard G, Royant A, Hink MA, Gadella TWJ, Jr. 2017. mScarlet: a bright monomeric red fluorescent protein for cellular imaging. Nat Methods 14:53–56. https://doi.org/10.1038/nmeth.4074.
56. Maekawa M, Fairn GD. 2015. Complementary probes reveal that phosphatidylserine is required for the proper transbilayer distribution of cholesterol. J Cell Sci 128:1422–1433. https://doi.org/10.1242/jcs.164715.
57. Wilhelm LP, Voilquin L, Kobayashi T, Tomasetto C, Alpy F. 2019. Intracellular and plasma membrane cholesterol labeling and quantification using filipin and GFP-D4. Methods Mol Biol 1949:137–152. https://doi.org/10.1007/978-1-4939-9136-5_11.
58. Jaqaman K, Loerke D, Mettlen M, Kuwata H, Grinstein S, Schmid SL, Danuser G. 2008. Robust single-particle tracking in live-cell time-lapse sequences. Nat Methods 5:695–702. https://doi.org/10.1038/nmeth.1237.